

# Momentum Distribution as a Fingerprint of Quantum Delocalization in Enzymatic Reactions: Open-Chain Path-Integral Simulations of Model Systems and the Hydride Transfer in Dihydrofolate Reductase

Hamutal Engel,<sup>†</sup> Dvir Doron,<sup>†</sup> Amnon Kohen,<sup>‡</sup> and Dan Thomas Major<sup>\*,†</sup>

<sup>†</sup>Department of Chemistry and the Lise Meitner–Minerva Center of Computational Quantum Chemistry, Bar-Ilan University, Ramat-Gan 52900, Israel

<sup>‡</sup>Department of Chemistry, University of Iowa, Iowa City, Iowa 52242, United States

**ABSTRACT:** The inclusion of nuclear quantum effects such as zero-point energy and tunneling is of great importance in studying condensed phase chemical reactions involving the transfer of protons, hydrogen atoms, and hydride ions. In the current work, we derive an efficient quantum simulation approach for the computation of the momentum distribution in condensed phase chemical reactions. The method is based on a quantum-classical approach wherein quantum and classical simulations are performed separately. The classical simulations use standard sampling techniques, whereas the quantum simulations employ an open polymer chain path integral formulation which is computed using an efficient Monte Carlo staging algorithm. The approach is validated by applying it to a one-dimensional harmonic oscillator and symmetric double-well potential. Subsequently, the method is applied to the dihydrofolate reductase (DHFR) catalyzed reduction of 7,8-dihydrofolate by nicotinamide adenine dinucleotide phosphate hydride (NADPH) to yield S-5,6,7,8-tetrahydrofolate and NADP<sup>+</sup>. The key chemical step in the catalytic cycle of DHFR involves a stereospecific hydride transfer. In order to estimate the amount of quantum delocalization, we compute the position and momentum distributions for the transferring hydride ion in the reactant state (RS) and transition state (TS) using a recently developed hybrid semiempirical quantum mechanics–molecular mechanics potential energy surface. Additionally, we examine the effect of compression of the donor–acceptor distance (DAD) in the TS on the momentum distribution. The present results suggest differential quantum delocalization in the RS and TS, as well as reduced tunneling upon DAD compression.

## INTRODUCTION

The transfer of protons, hydrogens, and hydride ions is ubiquitous in nature. In order to accurately treat this phenomenon theoretically, it is essential to account for nuclear quantum effects (NQE). NQEs such as zero-point energy and tunneling are due to the long de Broglie wavelength of the hydrogen atom, which is a result of its light mass. In particular, the inclusion of NQE in the theoretical treatment of enzyme catalysis is essential.<sup>1</sup> The importance of quantum mechanical (QM) tunneling in enzyme catalysis is a question of great debate. It has been proposed that enzymes have evolved to enhance tunneling in hydrogen transfer reactions by employing finely tuned vibrational modes that serve to bring the hydrogen donor and acceptor atoms to an optimal reactive state. In this view, tunneling may be used as a measure of protein motion that can be directly linked to catalysis, thereby enhancing our understanding of how enzymes make and break bonds.<sup>2</sup>

A universal feature of quantum effects is a wider position distribution than what is expected from purely classical consideration. Similarly, the classical and quantum description of the momentum distribution differ considerably, as the Gibbs classical momentum distribution is independent of the potential energy surface (PES).<sup>3</sup> Therefore, it is expected that NQE in general and tunneling in particular may be studied by analyzing the momentum distribution. Moreover, the nature of the PES may be scrutinized by analysis of the momentum distribution.

The hydrogen momentum distribution contains important information regarding the PES the hydrogen experiences in

condensed phase environments. The population of low momentum regions corresponds to rotational motion, librational motion, and low-frequency vibrational modes, while the high momentum regions correspond to bond stretching modes. Experimentally, the momentum distribution may be determined from neutron Compton scattering experiments, wherein high energy neutrons are scattered by the hydrogen atoms in the system. This yields a scattering cross-section that may be related to the momentum distribution.<sup>4,5</sup> Momentum distribution has been employed as a reporter of tunneling in several systems such as ferroelectric potassium dihydrogen phosphate,<sup>6</sup> water in various phases,<sup>7–9</sup> water confined in silica pores<sup>10</sup> or nanotubes,<sup>6</sup> superprotonic conductors,<sup>11</sup> and the hydration shell of globular proteins.<sup>12</sup> An unusual feature in the momentum distribution in these systems is the presence of secondary peaks, or shoulders, in regions of high momentum. These features have been attributed to nodes in the momentum distribution, and studies of model systems have suggested that these are related to ground state tunneling. Momentum distribution has also been obtained by numerous molecular simulations.<sup>13–19</sup>

In the current work, we derive a practical formulation for open chain polymer PI simulations in condensed phase chemical reactions. The method is based on a quantum-classical approach wherein quantum and classical simulations

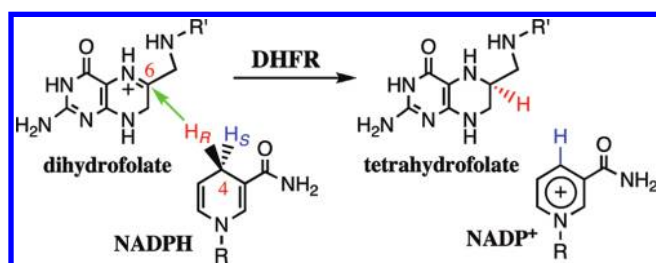
**Received:** December 6, 2011

**Published:** March 14, 2012



are performed separately. The classical simulations use standard sampling techniques, whereas the quantum simulations employ an open polymer chain path integral formulation which is computed using an efficient Monte Carlo (MC) staging algorithm. The approach, termed quantum-classical open path integrals (QCOPI), is validated by applying it to a one-dimensional harmonic oscillator and symmetric double well potential. Subsequently, the method is used to study the dihydrofolate reductase (DHFR) catalyzed reduction of 7,8-dihydrofolate ( $H_2$ folate) by nicotinamide adenine dinucleotide phosphate hydride (NADPH) to yield S-5,6,7,8-tetrahydrofolate ( $H_4$ folate) and  $NADP^+$ . The key chemical step in the catalytic cycle of DHFR involves a stereospecific transfer of the pro-R hydrogen at the C4 position of the nicotinamide ring in NADPH to the *si*-face of the C6 atom of the N5-protonated pterin ring in  $H_2$ folate (Scheme 1). The hydride transfer in

**Scheme 1. The Hydride Transfer Reaction Catalyzed by DHFR<sup>a</sup>**



<sup>a</sup>R: adenine dinucleotide 2'-phosphate. R': *p*-aminobenzoyl-glutamate.

DHFR has been studied extensively both experimentally<sup>20–27</sup> and computationally,<sup>28–37</sup> and the role of NQE has been well established. Herein, we employ the QCOPI approach to compute position and momentum distributions for the DHFR catalyzed hydride transfer reaction using a recently developed hybrid semiempirical quantum mechanics–molecular mechanics (QM/MM) potential energy surface.<sup>36</sup> The position distribution and momentum distribution are computed for the transferring atom in the reactant state (RS) and transition state (TS). Additionally, we examine the effect of compression of the donor–acceptor distance in the TS on the momentum distribution. The currently developed method is expected to be useful in the study of both solution and enzyme reactions, in conjunction with other PI approaches described previously.<sup>38–44</sup>

## THEORY

**Momentum and Position Distribution.** The one-dimensional position distribution for a single particle may be defined as

$$n_x(x) = \frac{1}{Q} \sum_{i=0}^{\infty} e^{-\beta E_i} |\psi_i(x)|^2 \quad (1)$$

where the partition function,  $Q$ , is defined as  $Q = \sum_{i=0}^{\infty} \exp(-\beta E_i)$ ,  $x$  is the position,  $\psi_i$  is the eigenfunction in position representation and  $E_i$  is the eigenvalue of state  $i$ . Analogously,

the one-dimensional momentum distribution for a single particle,  $n_p(p)$ , may be defined as follows:<sup>15</sup>

$$n_p(p) = \frac{1}{Q} \sum_{i=0}^{\infty} e^{-\beta E_i} |\phi_i(p)|^2 \quad (2)$$

where  $p$  is the momentum and  $\phi_i$  is the eigenfunction in momentum representation. Alternatively, the momentum distribution may be defined in terms of the thermal density matrix,  $\rho$ , as

$$\begin{aligned} n_p(p) &= \frac{1}{2\pi\hbar} \iint dx dx' \exp\left[-\frac{i}{\hbar} p(x - x')\right] \rho(x, x') \\ &= \frac{1}{2\pi\hbar} \int dR \exp\left[-\frac{i}{\hbar} pR\right] n(R) \end{aligned} \quad (3)$$

where  $\hbar$  is the reduced Planck's constant and  $\rho(x, x')$  is the one-dimensional thermal density matrix in position representation for a single particle. The distance distribution,  $n(R)$ , is defined as

$$n(R) = \iint dx dx' \delta(x - x' - R) \rho(x, x') \quad (4)$$

For the simulation of the momentum distribution described above in eq 3, it is necessary to sample off-diagonal elements of the density matrix. This may be achieved employing discrete Feynman path integral (PI) simulations.<sup>45,46</sup> In this PI description, the distance distribution,  $n(R)$ , is the end-to-end distance distribution of an open polymer chain. The partition function,  $Q$ , may be computed employing a closed polymer chain.

Alternatively, we may write the momentum distribution for the three-dimensional case using a form which is readily amendable to PI simulations:

$$n_p(p) = \left(\frac{1}{2\pi\hbar}\right)^3 \int g(R) \frac{\sin(pR/\hbar)}{pR/\hbar} dV \quad (5)$$

where  $dV = 4\pi R^2 dR$  and the end-to-end radial distribution function,  $g(R)$ , is defined as

$$g(R) \cong \frac{\langle \delta(|\mathbf{r} - \mathbf{r}'| - R) \rangle}{4\pi R^2} \quad (6)$$

where  $\mathbf{r}$  is the single particle position vector in three dimensions. In eq 5, the end-to-end radial distribution function is multiplied by a zeroth-order spherical Bessel function of the first kind. The ensemble averaged end-to-end distance of the open chain polymer requires the simulation of an open path of  $P + 1$  beads, i.e., discrete points along the Feynman path. A crucial question is how to obtain this ensemble averaged quantity.

Herein, we start with a general expression for the ensemble averaged end-to-end distance of a single quantum particle in a classical bath. We have previously shown that quantizing a single particle in a classical bath is a reasonable approximation for proton transfer reactions.<sup>38,39</sup> The bath coordinates are described by a collective variable,  $\mathbf{S}$ . The centroid position of the quantum particle is described by  $\mathbf{r}_c$  and the discrete points along the Feynman path are defined by  $\mathbf{r}_i$ . We may thus write

$$\langle \delta(|\mathbf{r}_i - \mathbf{r}_{P+1}| - R) \rangle = \frac{\int d\mathbf{S} \int d\mathbf{r}_c \int d\mathbf{R} \prod_{i=1}^P \rho(\mathbf{r}_i, \mathbf{r}_{i+1}; \tau, \mathbf{S}) \delta(|\mathbf{r}_i - \mathbf{r}_{P+1}| - R)}{\int d\mathbf{S} \int d\mathbf{r}_c \int d\mathbf{R} \prod_{i=1}^P \rho(\mathbf{r}_i, \mathbf{r}_{i+1}; \tau, \mathbf{S})} \quad (7)$$

where the integral over the path is defined as  $\int d\mathbf{R} = \int d\mathbf{r}_1 \dots \int d\mathbf{r}_{P+1} \delta(\bar{\mathbf{r}} - \mathbf{r}_c)$  and the path centroid is defined as  $\bar{\mathbf{r}} = [(\mathbf{r}_1 + \mathbf{r}_{P+1})/2 + \sum_{i=2}^P \mathbf{r}_i]/P$ . The thermal density matrix within the primitive approximation is defined as

$$\rho(\mathbf{r}_i, \mathbf{r}_{i+1}; \tau, \mathbf{S}) \cong \rho_V(\mathbf{r}_i; \tau/2, \mathbf{S}) \rho_T(\mathbf{r}_i, \mathbf{r}_{i+1}; \tau) \rho_V(\mathbf{r}_{i+1}; \tau/2, \mathbf{S}) \quad (8)$$

where  $\tau = \beta/P$ ,  $\rho_T$  is the kinetic energy ( $T$ ), i.e. free particle term for an open polymer chain:

$$\rho_T(\mathbf{r}_i, \mathbf{r}_{i+1}; \tau) = \Omega \exp\left[-\tau \frac{m}{2\tau^2 \hbar^2} (\mathbf{r}_i - \mathbf{r}_{i+1})^2\right] \quad (9)$$

where  $\Omega = [m/(2\pi\tau\hbar^2)]^{1/2}$  and  $m$  is the mass of the quantum particle.  $\rho_V$  is the potential energy ( $V$ ) term:

$$\rho_V(\mathbf{r}_i; \tau, \mathbf{S}) = \exp[-\tau V^{\text{QM}}(\mathbf{r}_i, \mathbf{S})] \quad (10)$$

where  $V^{\text{QM}}(\mathbf{r}_i, \mathbf{S})$  is the potential at time slice  $i$ :

$$V^{\text{QM}}(\mathbf{r}_i, \mathbf{S}) = \begin{cases} \frac{U(\mathbf{r}_1, \mathbf{S}) + U(\mathbf{r}_{P+1}, \mathbf{S})}{2} & i = 1 \\ U(\mathbf{r}_i, \mathbf{S}) & i = 2, \dots, P \end{cases} \quad (11)$$

Here  $U(\mathbf{r}_i, \mathbf{S})$  is the potential energy surface of the system. To allow rapid simulation of the end-to-end distance, we define the following semiclassical (SC) reference system:

$$\rho^{\text{SC}}(\mathbf{r}_i, \mathbf{r}_{i+1}; \tau, \mathbf{S}) \cong \rho_T(\mathbf{r}_i, \mathbf{r}_{i+1}; \tau) \rho_V^{\text{CM}}(\mathbf{r}_i; \beta, \mathbf{S}) \quad (12)$$

where the kinetic term was defined above and the centroid classical mechanics (CM) potential term is defined as

$$\rho_V^{\text{CM}}(\mathbf{r}_i; \beta, \mathbf{S}) = \exp[-\beta U(\mathbf{r}_c, \mathbf{S})] \quad (13)$$

An associated SC open-chain PI configuration integral may be defined as

$$I^{\text{SC}} = \int d\mathbf{S} \int d\mathbf{r}_c \rho_V^{\text{CM}}(\mathbf{r}_c; \beta, \mathbf{S}) \int d\mathbf{R} \prod_{i=1}^P \rho_T(\mathbf{r}_i, \mathbf{r}_{i+1}; \tau) \quad (14)$$

Let us insert the identity expression  $I^{\text{SC}}/I^{\text{SC}}$  into eq 7

$$\begin{aligned} \langle \delta(|\mathbf{r}_1 - \mathbf{r}_{P+1}| - R) \rangle = & \frac{\int d\mathbf{S} \int d\mathbf{r}_c \int d\mathbf{R} \prod_{i=1}^P \rho_V(\mathbf{r}_i; \tau/2, \mathbf{S}) \rho_T(\mathbf{r}_i, \mathbf{r}_{i+1}; \tau) \rho_V(\mathbf{r}_{i+1}; \tau/2, \mathbf{S}) \delta(|\mathbf{r}_1 - \mathbf{r}_{P+1}| - R)}{\int d\mathbf{S} \int d\mathbf{r}_c \rho_V^{\text{CM}}(\mathbf{r}_c; \beta, \mathbf{S}) \int d\mathbf{R} \prod_{i=1}^P \rho_T(\mathbf{r}_i, \mathbf{r}_{i+1}; \tau)} \\ & \frac{\int d\mathbf{S} \int d\mathbf{r}_c \int d\mathbf{R} \prod_{i=1}^P \rho_V(\mathbf{r}_i; \tau/2, \mathbf{S}) \rho_T(\mathbf{r}_i, \mathbf{r}_{i+1}; \tau) \rho_V(\mathbf{r}_{i+1}; \tau/2, \mathbf{S})}{\int d\mathbf{S} \int d\mathbf{r}_c \rho_V^{\text{CM}}(\mathbf{r}_c; \beta, \mathbf{S}) \int d\mathbf{R} \prod_{i=1}^P \rho_T(\mathbf{r}_i, \mathbf{r}_{i+1}; \tau)} \end{aligned} \quad (15)$$

Now, we insert the identity expression  $\rho_V^{\text{CM}}(\mathbf{r}_c; \beta, \mathbf{S})/\rho_V^{\text{CM}}(\mathbf{r}_c; \beta, \mathbf{S})$  to yield

$$\langle \delta(|\mathbf{r}_1 - \mathbf{r}_{P+1}| - R) \rangle = \frac{\left\langle \left\langle w \cdot \delta(|\mathbf{r}_1 - \mathbf{r}_{P+1}| - R) \right\rangle_{T, \mathbf{r}_c} \right\rangle_U}{\left\langle \left\langle w \right\rangle_{T, \mathbf{r}_c} \right\rangle_U} \quad (16)$$

where we have defined the weighting factor,  $w$ , as

$$w = \exp\left(-\frac{\beta}{P} \left( \frac{U(\mathbf{r}_1, \mathbf{S}) + U(\mathbf{r}_{P+1}, \mathbf{S}) - 2U(\mathbf{r}_c, \mathbf{S})}{2} + \sum_{i=2}^P [U(\mathbf{r}_i, \mathbf{S}) - U(\mathbf{r}_c, \mathbf{S})] \right)\right) \quad (17)$$

In the above expression, the end-to-end distribution may be obtained by a double averaging strategy.<sup>38,39,47,48</sup> The external average represents an average over the classical potential energy surface, which may be treated by molecular mechanics (MM), electronic structure QM methods, or hybrid QM/MM methods.<sup>49</sup> The internal averaging is over the kinetic, free-particle term, which is constrained to the centroid (i.e., classical) nuclear positions. In the above expression, the end-to-end distribution which is obtained from a free-particle distribution is weighted by the Boltzmann factored difference between the nuclear QM surface and the nuclear CM surface.

We note that the above expression describes a quantized particle in a bath of classical atoms. In reality, all bath particles should be quantized, i.e., treated by closed polymer PIs. Nonetheless, the current treatment should give useful qualitative insight into the position and momentum distribution in complex environments. Previously, we and other researchers have shown that one may treat a single quantized particle in the bath of classical particles in proton, hydrogen, and hydride transfer reactions with great success.<sup>33,38,39</sup>

**Staging Algorithm for Open Chain PI.** In order to implement the above method, we employ the staging algorithm<sup>50</sup> for open chain PI simulations.<sup>13,15</sup> Previously, we have employed the staging algorithm for the prediction of kinetic isotope effects using mass-perturbation simulations.<sup>44</sup> Here, we present a description of the open chain PI staging algorithm for free particle sampling, which may be readily implemented. The starting point is the free particle density matrix, which is described above in eq 9.

Assuming we want to sample  $P - 1$  discrete points along the Feynman path (termed beads) using the staging algorithm,  $\{\mathbf{r}_2, \dots, \mathbf{r}_P\}$ , between end points  $\mathbf{r}_1$  and  $\mathbf{r}_{P+1}$ , we define  $\mathbf{r}_1 = 0$  and  $\mathbf{r}_{P+1} = P^{1/2} \Lambda_m \boldsymbol{\eta}_0 = P^{1/2} \Lambda_m \boldsymbol{\theta}_0$ . Here, we define  $\Lambda_m = (2\pi\Omega^2)^{-1/2}$ , and  $\boldsymbol{\eta}_i$  is a random number vector with normal distribution, zero mean, and unit variance.

**Stage 1:**

$$\begin{aligned} \mathbf{r}_2 = & (\mathbf{r}_{P+1} + \mathbf{r}_1(P - 1))/P \\ & + \Lambda_m \boldsymbol{\eta}_1 \{(P - 1)/P\}^{1/2} = \Lambda_m [P^{1/2} \boldsymbol{\theta}_0/P + \boldsymbol{\theta}_1] \end{aligned} \quad (18)$$

where  $\boldsymbol{\theta}_1 = \boldsymbol{\eta}_1 \{(P - 1)/P\}^{1/2}$ .

**Stage 2:**

$$\begin{aligned} \mathbf{r}_3 = & (\mathbf{r}_{P+1} + \mathbf{r}_2(P - 2))/(P - 1) \\ & + \Lambda_m \boldsymbol{\eta}_2 \{(P - 2)/(P - 1)\}^{1/2} \\ = & \Lambda_m [(P^{1/2} \boldsymbol{\theta}_0 + (\mathbf{r}_2/\Lambda_m)(P - 2))/(P - 1) \\ & + \boldsymbol{\theta}_2] \end{aligned} \quad (19)$$

where  $\boldsymbol{\theta}_2 = \boldsymbol{\eta}_2 \{(P - 2)/(P - 1)\}^{1/2}$ .

Stage 3:

$$\begin{aligned} \mathbf{r}_4 &= (\mathbf{r}_{P+1} + \mathbf{r}_3(P-3))/(P-2) \\ &\quad + \Lambda_m \eta_3 \{ (P-3)/(P-2) \}^{1/2} \\ &= \Lambda_m [ (P^{1/2} \theta_0 + (\mathbf{r}_3/\Lambda_m)(P-3))/(P-2) \\ &\quad + \theta_3 ] \end{aligned} \quad (20)$$

where  $\theta_3 = \eta_3 \{ (P-3)/(P-2) \}^{1/2}$ .

Stage  $k-1$ :

$$\begin{aligned} \mathbf{r}_k &= \Lambda_m [ (P^{1/2} \theta_0 + (\mathbf{r}_{k-1}/\Lambda_m)(P-k+1)) \\ &\quad / (P-k+2) + \theta_{k-1} ] \end{aligned} \quad (21)$$

where  $\theta_{k-1} = \eta_{k-1} \{ (P-k+1)/(P-k) \}^{1/2}$ .

## ■ COMPUTATIONAL DETAILS

To assess the new method, we compute the momentum distribution, as well as the position distribution, for two model systems and for the DHFR catalyzed hydride transfer reaction.

**Model Systems.** In order to test the new QCOPI open-path integral method, we apply it to two simple model systems: the harmonic oscillator (HO) and a symmetric double well (SDW) potential. To assess the accuracy of the QCOPI method, we benchmark against the exact momentum distribution computed directly with two complementary approaches: using the eigenfunctions and eigenvalues (eq 2) or using the exact density matrix (eq 3). The exact density matrix (eq 3) is obtained by applying the iterative scheme for numerical matrix multiplication (NMM).<sup>51–53</sup> The NMM method allows rapid analysis of the momentum distribution convergence as a function of the number of beads and avoids the numerical noise inherent to simulation methods. We also employ density matrix diagonalization (DMD), which gives the eigenvalues and eigenvectors of the density matrix (eq 2) as well as the trace, as an alternative to NMM.<sup>54</sup> The momentum distributions obtained using the complementary NMM and DMD methods are then used to compare results obtained using the one-dimensional version of eq 5 in conjunction with the QCOPI method (eq 16). Specifically, within the QCOPI approach, we perform Monte Carlo (MC) sampling for the classical simulation and use the staging algorithm for the open path integral free particle sampling. The model calculations used 256 beads, unless otherwise stated. Approximately 100 000 MC steps were used for the classical configuration sampling, and 1000 MC staging steps per classical configuration were employed in computing the momentum distribution for the model systems.

The HO is given by

$$V_{\text{HO}}(x) = ax^2 \quad (22)$$

where we have employed a force constant of  $a = 309 \text{ kcal} \cdot \text{mol}^{-1} \cdot \text{\AA}^{-2}$ , which models a typical force field value for a C–H bond, and we use the mass of a hydrogen atom.

The SDW is given by

$$V_{\text{SDW}}(x) = ax^4 + bx^2 + c \quad (23)$$

where we have employed a mass of  $1224.259m_e$  (where  $m_e$  is the mass of an electron),  $a = 0.01 \text{ au}$ ,  $b = -0.01 \text{ au}$ , and  $c = 0.0025 \text{ au}$ .<sup>44</sup> Using these parameters, the barrier height is  $1.57 \text{ kcal/mol}$ .

**DHFR Catalyzed Hydride Transfer.** *Model of the Enzyme–Substrate–Coenzyme Complex.* The initial coordinates used to build the model for the present study were based on the crystal structure of a complex of *E. coli* DHFR with folate, NADP<sup>+</sup>, and water molecules (PDB ID code 1RX2<sup>55</sup>), where the Met20 loop is in the closed conformation. In this complex, the distance between the H-donor and H-acceptor atoms is short, and the reactive fragments have the correct regio- and stereochemistry. This structure is therefore commonly used as a mimic for the reactive ground state.<sup>28–37</sup> The original ligands in this structure were exchanged by N5-protonated H<sub>2</sub>folate and NADPH. Out of the 159 amino acid residues, all ionizable residues were treated as bearing protonation states that match neutral pH.<sup>20–22</sup> In particular, Asp27 was modeled as deprotonated,<sup>56–58</sup> and the specific protonation states of the histidine residues were determined on the basis of hydrogen bonding interactions. This model was soaked in a pre-equilibrated  $65 \times 65 \times 65 \text{ \AA}^3$  cubic water box and thereafter neutralized by adding 14 sodium ions to allow evaluation of electrostatic interactions using the Ewald summation scheme. The final model is comprised of 27 986 atoms. Further details are provided in our introductory study.<sup>36</sup>

**Potential Energy Surface.** The PES in the current study is described by a hybrid QM/MM Hamiltonian.<sup>59,60</sup> The QM region consists of 69 atoms, including portions of the substrate and coenzyme that are in proximity to the reaction center, and two link atoms. This part is described by a modified AM1 semiempirical Hamiltonian,<sup>61</sup> where the parameters have been optimized to treat model reactions involving various derivatives of nicotinamide and pterin compounds (specific reaction parameters, denoted AM1-SRP).<sup>36</sup> The MM part contains the protein; the remaining substrate and coenzyme atoms which are not described by QM; ions, all treated by the CHARMM22/27 force field<sup>62</sup> with grid-based energy correction maps (CMAP)<sup>63</sup> for peptide dihedral angles; and water molecules, which are represented by the three-point charge TIP3P model.<sup>64</sup> QM/MM interactions were treated by electrostatic embedding wherein the MM partial atomic charges are included in the one-electron Hamiltonian. QM/MM interaction energies between the reacting fragments (QM) and the protein (MM) were fine-tuned by modifying the van der Waals parameters of the QM hydrogen atoms.<sup>65</sup> This combined potential energy was shown to yield an accuracy comparable to density functional theory (DFT), giving accurate results for the hydride transfer reaction in *ec*DHFR.<sup>36</sup> Our previous work contains a detailed QM/MM partitioning scheme as well as a thorough description of the development of the AM1-SRP Hamiltonian.<sup>36</sup>

**Molecular Dynamics Simulations.** Periodic boundary conditions (PBC) were applied, and the Ewald method was employed for reciprocal space summations between MM sites as well as for the QM/MM interactions ( $64 \times 64 \times 64$  FFT grid,  $\kappa = 0.340 \text{ \AA}^{-1}$ ).<sup>66</sup> A  $13.0 \text{ \AA}$  group-based cutoff was applied for van der Waals and electrostatic interactions. The isothermal–isobaric (NPT) ensemble was employed at 298 K and 1 atm using the extended pressure/temperature (CPT) algorithm<sup>67</sup> with a Hoover thermostat.<sup>68</sup> The leapfrog integration scheme<sup>69</sup> was used to propagate the equations of motion, and the SHAKE algorithm<sup>70</sup> was applied to constrain all MM bonds involving hydrogen atoms, allowing a time step of 1 fs. The system was heated up in a stepwise fashion from 48 to 298 K for 25 ps and thereafter equilibrated at the target temperature (298 K) over the course of 1 ns at the MM level of



theory, with a further 200 ps of equilibration using the QM(AM1-SRP)/MM potential. Further details of the molecular dynamics (MD) simulations are available in our earlier work.<sup>36</sup>

**QCOPI Simulations.** The classical-mechanical potential of mean force (CM-PMF)<sup>71</sup> was determined using the umbrella sampling technique, in order to sample the high-energy regions of the potential energy surface.<sup>72</sup> The reaction coordinate ( $\zeta$ ) was defined geometrically as the difference between the lengths of the breaking C4N–H and forming H–C6 bonds. A total of 16 discrete regions along the reaction coordinate (“windows”) were defined with a uniform spacing of 0.25 Å. Each simulation was performed with the addition of a biasing potential (roughly the negative of the computed PMF), and a harmonic restraint centered at each window. The harmonic force constants,  $k$ , ranged between 20.0 and 60.0 kcal·mol<sup>−1</sup>·Å<sup>−2</sup> [ $E_{\text{harm}} = k(\zeta - \zeta_{\text{ref}})^2$ ]. The QM-PMF was obtained by quantizing a subset of atoms in the chemically reactive region using closed polymer ring path-integral simulations.<sup>36</sup> In this description, the reaction coordinate is defined analogously to the classical case, but with the ring polymer centroid positions replacing the classical positions.<sup>41</sup> On the basis of the QM-PMF, we define the reactant state (RS) and transition state (TS) as ensembles of structures in the reactant well and at the dividing surface, respectively. The trajectories in the RS and TS obtained from PMF simulations were employed in the QCOPI simulations to get the momentum distribution and open path end-to-end distance. The open paths were represented by  $P = 32$  (i.e., 33 beads). The QCOPI code may perform either anisotropic sampling or isotropic sampling (i.e., end to end distance sampling along a predefined direction). Approximately 10 000 classical configurations and 100 MC staging steps were employed in computing the momentum distribution for each state along the reaction coordinate according to eq 16.

All enzyme simulations used a development version of the CHARMM program.<sup>73,74</sup>

## RESULTS AND DISCUSSION

In the present work, we report the momentum and position distribution for two simple model systems and the momentum distribution for the DHFR catalyzed reduction of H<sub>2</sub>folate by nicotinamide adenine dinucleotide phosphate hydride (NADPH) to yield H<sub>4</sub>folate and NADP<sup>+</sup>. For the two model systems, we employ both the new QCOPI and numerically exact NMM and DMD methods, while for the DHFR-catalyzed hydride transfer, we use the QCOPI approach.

**Temperature-Dependent Momentum Distribution for Model Systems. Harmonic Oscillator.** The position distribution and momentum distribution for the harmonic oscillator (eq 22) are computed using the NMM and DMD approaches described in the Computational Methods section. In Figure 1A, we present the position distribution of the harmonic oscillator at  $T = 100$ –400 K, 600 K, and 1000 K, while in Figure 1B we present the square of the eigenfunction at the four lowest quantum levels. It is discernible (Figure 1A and Table 1) that the position distribution becomes increasingly wider as the temperature is increased. This is most pronounced at the higher temperatures, where the higher energy levels become increasingly populated (Table 1). In Figure 1B, we present the squared wave functions for the four lowest energy levels, which are obtained with the DMD method. The position distribution in Figure 1A is obtained by combining the data in Figure 1B and Table 1 using eq 1. A

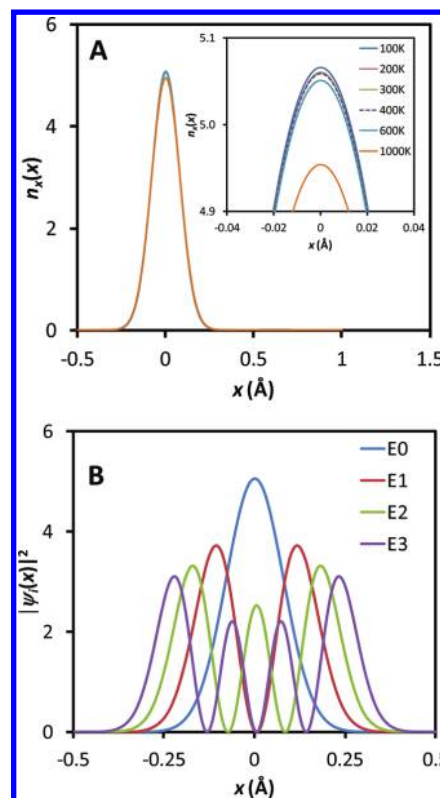


**Figure 1.** Numerical density matrix multiplication and density matrix diagonalization calculations for the harmonic oscillator. (A) Position distribution at selected temperatures. (B)  $|\psi_i(x)|^2$  for the four lowest eigenstates. The calculations used 256 beads.

**Table 1.** Eigenvalues (kcal/mol) and Probability Factors for the Harmonic Oscillator

level	$E_i$	$e^{-\beta E_i}/Q$					
		temperature (K)					
		100	200	300	400	600	1000
0	3.84	1.000	1.000	1.000	1.000	0.999	0.979
1	11.53	0.000	0.000	0.000	0.000	0.001	0.020
2	19.22	0.000	0.000	0.000	0.000	0.000	0.001
3	26.91	0.000	0.000	0.000	0.000	0.000	0.000

comparison of Figure 1A and B reveals that the ground level is primarily populated at all temperatures, and this is confirmed by inspection of the population of states in Table 1. In Figure 2, the momentum distribution data are presented. At the lowest temperature, the momentum distribution is peaked since lower momentum values are more likely. As the temperature is increased, the distribution widens as higher momentum values become more probable. The widest momentum distribution is observed at  $T = 1000$  K. In Figure 2B, we present the squared wave functions for the four lowest energy levels. The momentum distribution in Figure 2A is obtained by combining the data in Figure 2B and Table 1 using eq 2.

To test the QCOPI method, we compute the momentum distribution using the classical MC and PI staging approach described in the Computational Methods section. In Figure 3A, we present the momentum distribution obtained in the temperature range 100–1000 K using QCOPI. The simulation results are compared with the exact numerical results from the NMM/DMD methods described in the previous paragraph.

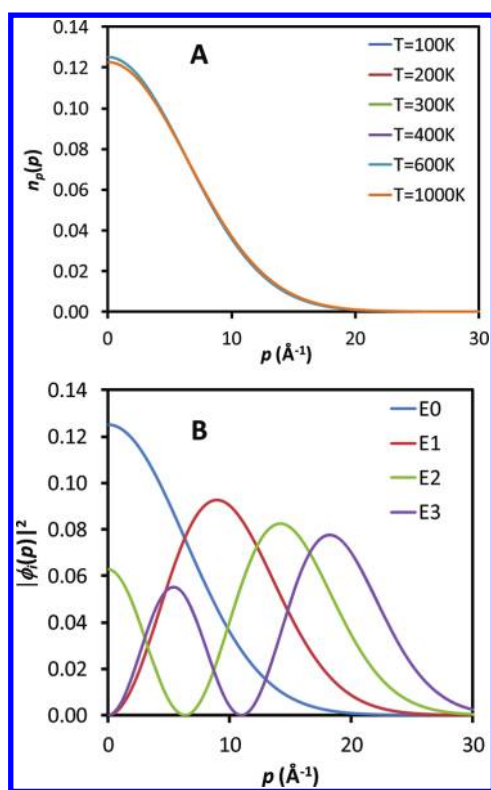


**Figure 2.** Numerical density matrix multiplication and density matrix diagonalization calculations for the harmonic oscillator. (A) Momentum distribution at selected temperatures. (B)  $|\phi_i(p)|^2$  for the four lowest eigenstates. The distributions have been normalized for positive values of  $p$ . The calculations used 256 beads.

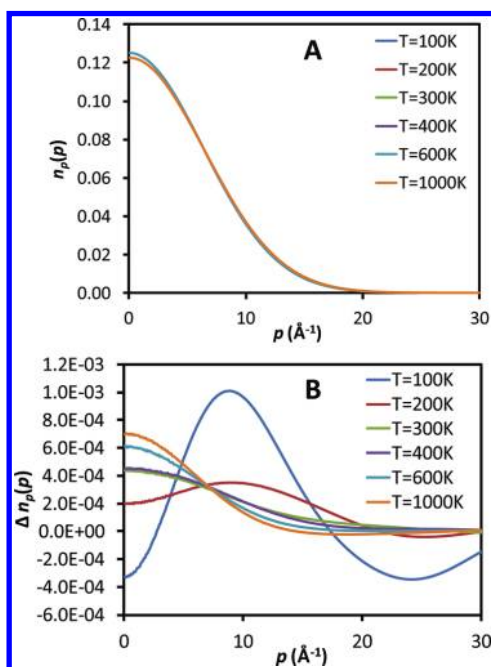


**Figure 3.** (A) Momentum distribution for the harmonic oscillator at selected temperatures computed using quantum-classical open path-integral simulations. (B) Difference between quantum-classical open path-integral simulations and numerical exact results. The distributions have been normalized for positive values of  $p$ . The calculations used 256 beads.

The difference between the NMM/DMD results and the QCOPI simulated results are minor (Figure 3B). The difference is greatest at lower temperatures and subsequently decreases as the temperature is increased. The maximum error in momentum distribution occurs at  $T = 100$  K and amounts to ca. 2%. The reason for the greater error at the lowest temperature is likely a difference in the classical and quantum configuration space. At a temperature of 100 K, the classical simulations are unable to sample high energy regions due to insufficient thermal energy, while quantum effects are considerable and particles may penetrate the wall of the harmonic oscillator. Since QCOPI quantum simulations are based on classically sampled configurations, high energy regions may be insufficiently sampled at low temperatures.

We further test the convergence for the QCOPI method as a function of the number of beads at a temperature of biological interest, namely, 300 K (Figure 4). The momentum

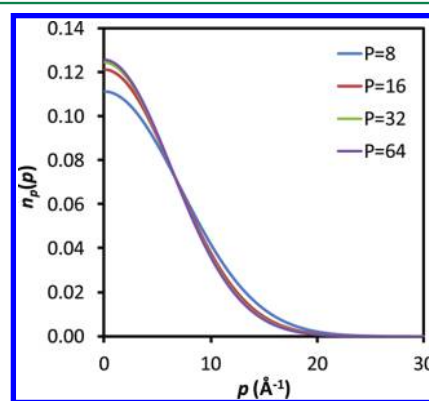


**Figure 4.** Momentum distribution for the harmonic oscillator computed using quantum-classical open path-integral simulations with  $P = 8, 16, 32$ , and  $64$ . The distributions have been normalized for positive values of  $p$ .

distribution is computed using  $P = 8, 16, 32$ , and  $64$ . Visual inspection of Figure 4 suggests that, using 8 and 16 beads, the distribution is somewhat wider than the 64 bead case, while when 32 beads are used, the results are well converged.

**Symmetric Double Well Potential.** The position distribution and momentum distribution for the symmetric double well potential (eq 23) are computed using the NMM and DMD approaches described in the Computational Methods section. In Figure 5A, we present the position distribution of the double well potential in the temperature range 100–1000 K, while in Figure 5B we show the square of the wave function at the four lowest quantum levels with the DMD method. The bimodal distributions observed suggest that barrier crossings occur at all temperatures. As suggested by Morrone et al., at low temperatures, only states below the barrier are populated, and barrier crossings are due to quantum tunneling.<sup>15</sup> As the temperature is increased, thermal crossing competes with quantum crossing, and at the higher temperature, the barrier crossings are largely due to classical behavior. In Table 2, we display the eigenvalues and probability factors for the symmetric double well potential. The ground state energy level is at 1.19 kcal/mol, which is the only energy level below the potential energy barrier (1.57 kcal/mol). At  $T = 100$  K, the ground state is nearly exclusively populated (Table 2), and the bimodal distribution seen in Figure 5B is largely due to ground state tunneling. As the temperature increases, the bimodal

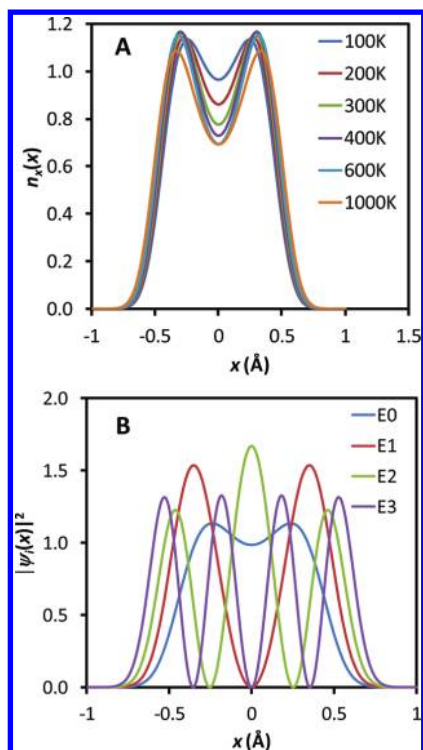


**Figure 5.** Numerical density matrix multiplication and density matrix diagonalization calculations for the symmetric double well potential. (A) Position distribution at selected temperatures. (B)  $|\psi_i(x)|^2$  for the four lowest eigenstates. The calculations used 256 beads.

**Table 2. Eigenvalues (kcal/mol) and Probability Factors for the Symmetric Double Well Potential**

level	$E_i$	$e^{-\beta E_i}/Q$					
		temperature (K)					
		100	200	300	400	600	1000
0	1.19	0.979	0.872	0.779	0.711	0.617	0.502
1	1.95	0.021	0.128	0.216	0.272	0.325	0.342
2	4.16	0.000	0.000	0.005	0.017	0.051	0.113
3	6.56	0.000	0.000	0.000	0.000	0.007	0.033

distribution includes additional contributions from higher energy levels, which have similar distributions to that of a harmonic oscillator.

To obtain complementary information to the position distribution, we employ the momentum distribution. In Figure 6A, we present the momentum distribution profiles in the temperature range 100–1000 K. At  $T = 100$  K, the system occupies primarily the ground state. The shape of the momentum distribution is narrow and decaying considerably faster than at the higher temperatures, resembling the features of  $|\phi_0(p)|^2$  (Figure 6B). An interesting feature at this temperature is the secondary peak which occurs at  $p > 6 \text{ Å}^{-1}$ , which is a fingerprint of tunneling.<sup>15</sup> Indeed, nodes in the momentum distribution of a one-dimensional system is indicative of tunneling, in the case of a potential with a barrier, combined with a bimodal position distribution.<sup>15</sup> At intermediate temperatures, one may observe secondary features, or shoulders, in the momentum distribution, as the ground state and excited states mix. These shoulders in the momentum distribution suggest the existence of tunneling. At  $T = 200$  K and  $T = 300$  K, we identify such secondary features in the

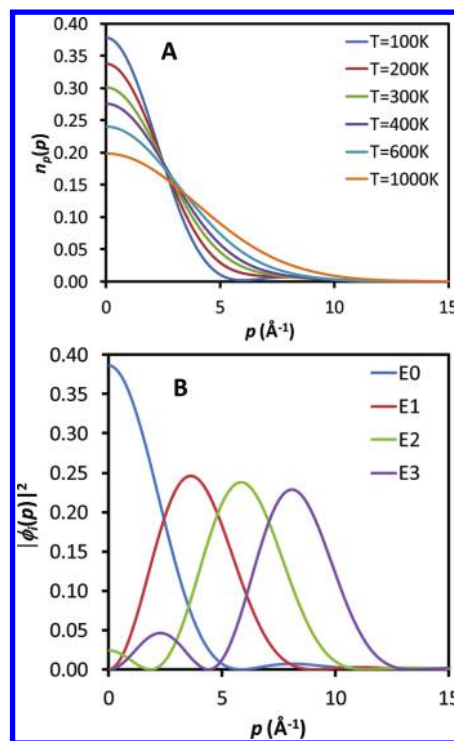


**Figure 6.** Numerical density matrix multiplication and density matrix diagonalization calculations for the symmetric double well potential. (A) Momentum distribution at selected temperatures. (B)  $|\phi_i(p)|^2$  for the four lowest eigenstates. The distributions have been normalized for positive values of  $p$ . The calculations used 256 beads.

momentum distribution where the momentum distribution has a long tail,<sup>15</sup> as levels above the barrier level are also occupied and compete with over the barrier processes. As the temperature is increased and higher energy levels occupied, the momentum distribution becomes increasingly wider, while the secondary peak disappears. At the higher temperatures, the distribution becomes increasingly Gaussian-like. The reasons for these trends are readily discernible by inspection of Figure 6B and Table 2. The momentum distribution at  $T = 100$  K (Figure 6A) is nearly identical to the momentum distribution obtained by evaluation of eq 2 with the ground level eigenfunction and eigenvalue (Figure 6B). Indeed, at this temperature, the ground level is nearly exclusively populated (Table 2). As the temperature is increased, the higher states are increasingly populated, causing a mixing of the ground state momentum distribution with those of higher states.

To test the QCOPI method, we compute the momentum distribution using the classical MC and PI staging approach described in the Computational Methods section and compare with the exact numerical results from NMM/DMD. In Figure 7A, we present the momentum distribution obtained in the temperature range 100–1000 K. The difference between the NMM/DMD results and the QCOPI simulated results is minor (Figure 7B). The difference is greatest at lower temperatures, and subsequently decreases as the temperature is increased. At  $T = 100$  K, the secondary peak obtained with QCOPI is slightly smaller than that with NMM/DMD. This is seen as a negative peak in the difference distribution in Figure 7B at  $p \approx 7 \text{ Å}^{-1}$ . The maximum absolute error in the momentum distribution occurs at  $T = 100$  K and at  $p \approx 3 \text{ Å}^{-1}$ , amounting to ca. 10%. The negative sign of  $n(p)$  at around  $6\text{--}7 \text{ Å}^{-1}$  (Figure 7A) is unphysical and is due to numerical errors. The reason for the



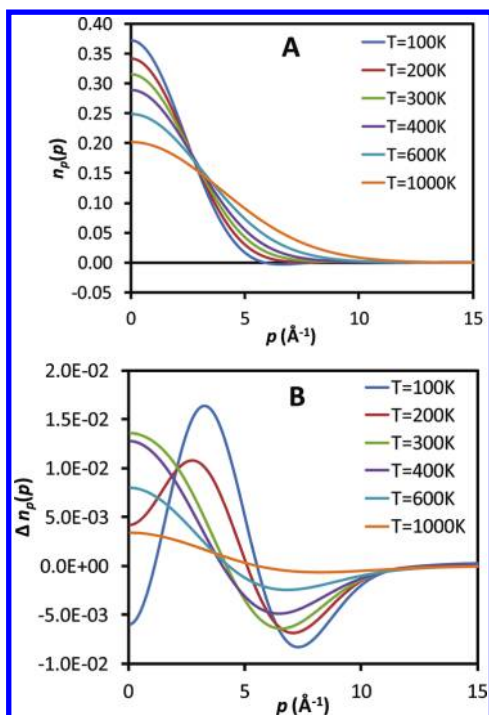


**Figure 7.** (A) Momentum distribution for the symmetric double well potential at selected temperatures computed using quantum-classical open path-integral simulations. (B) Difference between quantum-classical open path-integral simulations and numerical exact results. The distributions have been normalized for positive values of  $p$ . The calculations used 256 beads.

greater error at the lowest temperature is likely a significant difference in the classical and quantum configuration space. At a temperature of 100 K, the jumps between wells during the classical simulations are infrequent due to insufficient thermal energy, while quantum tunneling allows rapid barrier crossing.

We further test the convergence for the QCOPI method as a function of the number of beads at a temperature of 300 K (Figure 8). The momentum distribution is computed using  $P = 8, 16, 32$ , and  $64$ . Visual inspection of Figure 8 suggests that, when eight beads are used, the distribution is marginally wider than the 64 bead case, while when 16 and 32 beads are used, the results are well converged.

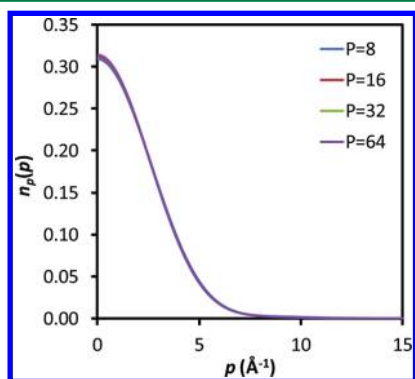


**Figure 8.** Momentum distribution for the symmetric double well potential computed using quantum-classical open path-integral simulations with  $P = 8, 16, 32$ , and  $64$ . The distributions have been normalized for positive values of  $p$ .

**Momentum Distribution in the DHFR Catalyzed Hydride Transfer.** We employ the QCOPI approach to assess the quantum delocalization in the DHFR catalyzed reduction of  $\text{H}_2\text{folate}$  by NADPH to yield  $\text{H}_4\text{folate}$  and  $\text{NADP}^+$  (Figure 9). In Figure 10, we present the end-to-end distribution

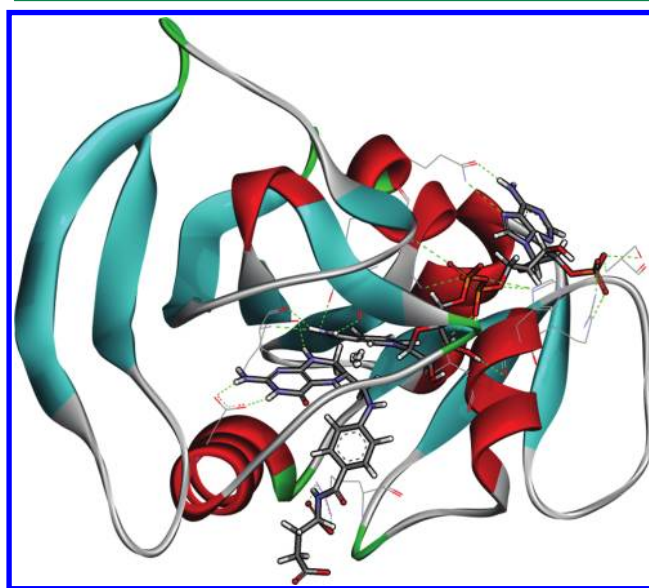


**Figure 9.** Snapshot of a transition state configuration in the hydride transfer reaction catalyzed by DHFR at  $T = 298$  K. The transferring hydride is described by an open chain path-integral composed of 32 beads.

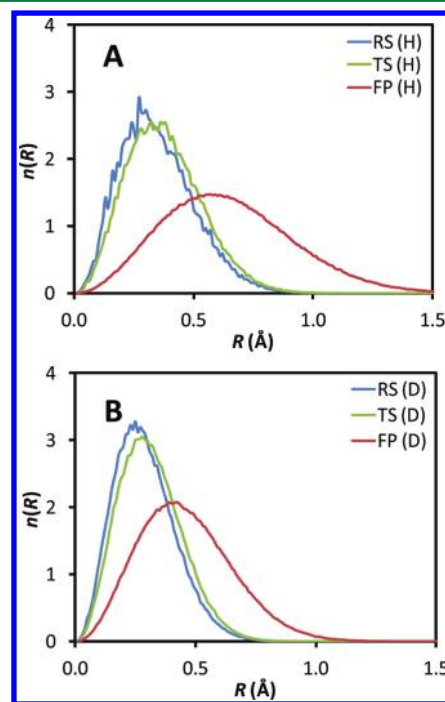


**Figure 10.** End-to-end distance distribution of the open polymer chain in the path integral simulation of the reactant state (RS) and transition state (TS) in the hydride (A) and deuteride (B) transfer reactions catalyzed by DHFR at  $T = 298$  K. The free-particle (FP) end-to-end distribution is added as a reference. The calculations used 32 beads.



in the RS and TS of the case of a hydride transfer (Figure 10A) and a deuteride transfer (Figure 10B). For comparison, the free particle end-to-end distribution of the Feynman path is also shown. In the case of a hydride transfer, we see that the ensemble averaged end-to-end distance is greater in the TS than in the RS, suggesting greater delocalization of the transferring hydride. The same effect is observed in the case of a deuteride transfer. Additionally, in both cases, the free-particle end-to-end distribution is considerably wider than in the presence of the external potential. A comparison of the hydride and the deuteride cases also suggests that the hydride path is more delocalized than the deuteride path, as is expected due to the mass difference. This is seen in the hydride and the deuteride end-to-end distributions in the RS and in the TS.

Complementary insight is obtained by studying the momentum distribution of the hydride and deuteride in the RS and TS (Figure 11). In the case of hydride transfer (Figure

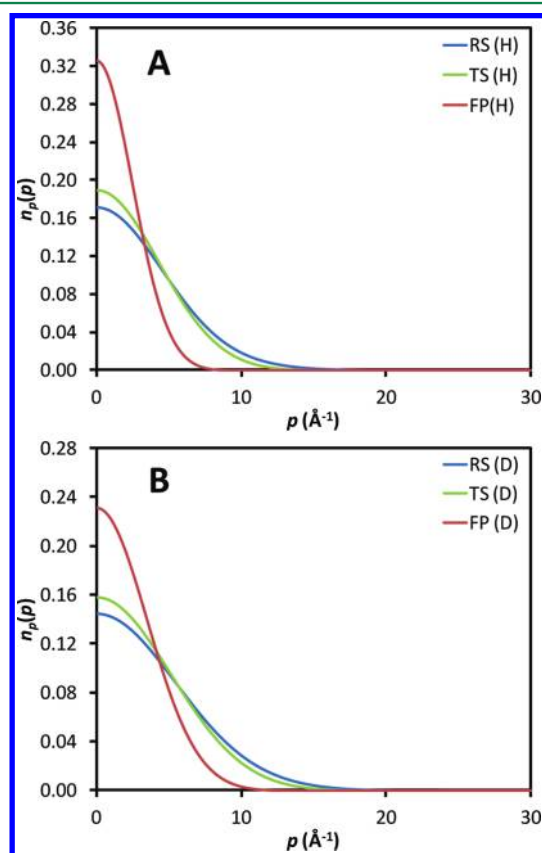


**Figure 11.** Anisotropic momentum distribution obtained from open polymer chain path integral simulation of the reactant state (RS) and transition state (TS) in the hydride (A) and deuteride (B) transfer reactions catalyzed by DHFR at  $T = 298$  K. The free-particle (FP) momentum distribution is added as a reference. The distributions have been normalized for positive values of  $p$ . The calculations used 32 beads.

11A), we see that the momentum distribution is considerably narrower in the TS than in the RS. This red shift in  $n(p)$  in the TS is expected as the C–H bond is partially broken and the corresponding bond frequency is reduced. We note that such differences in the momentum distribution in the RS and TS are due to differences in NQE in these states. Indeed, the isothermal classical momentum distribution is Maxwellian and does not depend on the nature of the interaction potential

between the particles (FP curve in Figure 11).<sup>3</sup> At a momentum of ca.  $15 \text{ Å}^{-1}$ , we observe a secondary feature, seen as a slight tail, which might be indicative of tunneling in the DHFR reaction. To deconvolute possible effects of anisotropy in the spherically averaged momentum distribution, we also compute the isotropic momentum distribution along the donor–acceptor direction. It is evident from Figure 12 that

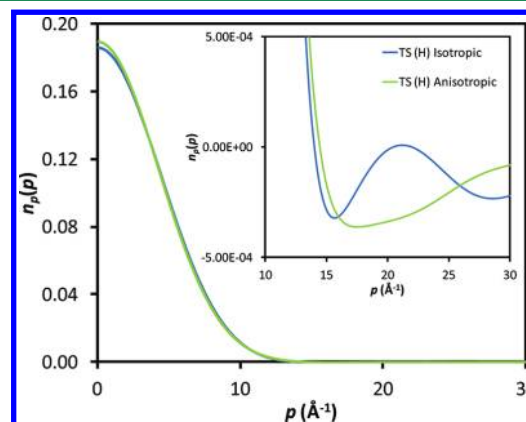


**Figure 12.** Isotropic and anisotropic momentum distributions obtained from open polymer chain path integral simulation of the transition state (TS) in the hydride transfer reaction catalyzed by DHFR at  $T = 298$  K. The distributions have been normalized for positive values of  $p$ . The calculations used 32 beads.

the secondary features in the momentum distribution are greater in the isotropic simulations. Considering the barrier in the underlying potential and the assumed bimodal distribution, these secondary features are indicative of tunneling.<sup>15</sup> This is in agreement with earlier work using semiclassical tunneling calculations.<sup>28</sup> The corresponding RS momentum distribution is wider in the case of hydride transfer. On the basis of the end-to-end distribution described earlier and the uncertainty principle, we would then suggest that the hydride is more delocalized in the TS than in the RS. This is also true in the deuteride case, although to a lesser extent, as an inspection of Figures 10 and 11 suggests. The momentum distribution in the RS and TS is wider for deuteride than for hydride (Figure 11A and B), as a result of the greater mass. Additionally, we see that the momentum distribution is narrower in the TS than in the RS for deuteride. This red shift in  $n(p)$  in the TS is due to the reduced bond frequency of the partially broken C–D bond.

To gain further insight into the potential experienced by the transferring hydride in the TS, we compute the momentum distribution at selected donor–acceptor distances (DAD; Figure 13): DAD =  $2.50 \text{ Å}$  and DAD =  $2.64 \text{ Å}$ . The latter DAD represents the TS. Such an analysis is expected to clarify the extent of quantum delocalization at the TS as a function of the enzyme environment. This topic has been addressed indirectly by several researchers—here, we provide direct evidence of the effect of DAD compression. An inspection of Figure 13 suggests that the momentum distribution is wider, and secondary features in the momentum distribution are depleted, at the shorter DAD. Thus, as the donor–acceptor distance is compressed further, the underlying barrier in the potential experienced by the hydride ion is reduced, and the hydride position becomes increasingly localized. In other words, the double well potential experienced by the hydride at greater donor–acceptor distances is reduced upon compression, as has been suggested by Warshel et al.<sup>75</sup>

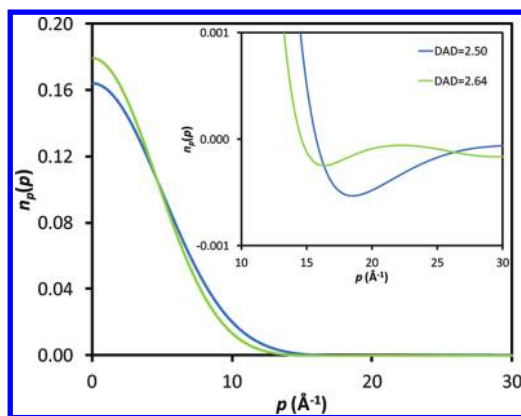


**Figure 13.** Isotropic momentum distributions obtained from open polymer chain path integral simulation of the transition state (TS) with different donor–acceptor distances (DAD) in the hydride transfer reaction catalyzed by DHFR at  $T = 298$  K. The distributions have been normalized for positive values of  $p$ . The calculations used 32 beads.

Interestingly, a similar trend has been observed in studies on the different forms of ice.<sup>76</sup>

## CONCLUSIONS

In the current work, we present a new method, termed QCOPI, which allows the computation of the momentum distribution in condensed phase reactions. The method is based on classical configurations which are used as a basin for quantum simulations. The quantum simulations employ open chain path integrals to estimate the chain end-to-end distribution. The polymer chain is sampled efficiently using the staging algorithm. The current method is tested on two model systems: the harmonic oscillator and a symmetric double well potential. The simulation results for these model systems are compared with results obtained using the numerical matrix multiplication method and the density matrix diagonalization method (Figures 3 and 7). Furthermore, the QCOPI approach is tested on the DHFR catalyzed hydride transfer reaction. The results suggest differential quantum delocalization in the reactant and transition states. On the basis of secondary features in the momentum distribution in the transition state, we suggest that tunneling might play a role in the DHFR catalyzed reaction. Furthermore, we suggest that compression of the donor–acceptor distance reduces tunneling. The current method has numerous favorable features which will be utilized in future studies of solution phase and enzyme reactions: (i) One may pinpoint quantum effects to specific atoms such as primary and secondary atoms in solution and enzyme catalysis, which enables focusing on atoms involved in chemical conversions. (ii) Quantum delocalization can be studied as a function of molecular configuration, as a new tool to assess NQE. (iii) Different isotopes may be studied, which could be instrumental in comparison to experimental isotope effect studies. (iv) Quantum delocalization can be studied as a function of the temperature and pressure, allowing comparison to experimental studies of temperature and pressure effects. (v) Dynamical effects in enzymes and (vi) energy distribution and dissipation can also be studied.

## AUTHOR INFORMATION

### Corresponding Author

\*E-mail: majort@biu.ac.il.

## Notes

The authors declare no competing financial interest.

## ACKNOWLEDGMENTS

This work has been supported by the Israel Science Foundation and the United States–Israel Binational Science Foundation (Grant # 2007256). We thank Prof. Kenneth Kay for helpful comments to the manuscript.

## REFERENCES

- (1) Pu, J. Z.; Gao, J. L.; Truhlar, D. G. Multidimensional tunneling, recrossing, and the transmission coefficient for enzymatic reactions. *Chem. Rev.* **2006**, *106*, 3140.
- (2) Nagel, Z. D.; Klinman, J. P. A 21st century revisionist's view at a turning point in enzymology. *Nat. Chem. Biol.* **2009**, *5*, 543.
- (3) Landau, L. D.; Lifshitz, E. M. *Statistical Physics*; Pergamon: Moscow, 1980; Vol. 1.
- (4) Mayers, J.; Reiter, G. F.; Platzman, P. Measurement of proton momentum distributions by eV neutron scattering. *J. Mol. Struct.* **2002**, *615*, 275.
- (5) Reiter, G. F.; Mayers, J.; Noreland, J. Momentum-distribution spectroscopy using deep inelastic neutron scattering. *Phys. Rev. B* **2002**, *65*, 104305.
- (6) Reiter, G. F.; Mayers, J.; Platzman, P. Direct Observation of Tunneling in KDP using Neutron Compton Scattering. *Phys. Rev. Lett.* **2002**, *89*, 135505.
- (7) Burnham, C. J.; Reiter, G. F.; Mayers, J.; Abdul-Redah, T.; Reichert, H.; Dosch, H. On the origin of the redshift of the OH stretch in Ice Ih: evidence from the momentum distribution of the protons and the infrared spectral density. *Phys. Chem. Chem. Phys.* **2006**, *8*, 3966.
- (8) Pantalei, C.; Pietropaolo, A.; Senesi, R.; Imberti, S.; Andreani, C.; Mayers, J.; Burnham, C.; Reiter, G. Proton Momentum Distribution of Liquid Water from Room Temperature to the Supercritical Phase. *Phys. Rev. Lett.* **2008**, *100*, 177801.
- (9) Pietropaolo, A.; Senesi, R.; Andreani, C.; Botti, A.; Ricci, M. A.; Bruni, F. Excess of Proton Mean Kinetic Energy in Supercooled Water. *Phys. Rev. Lett.* **2008**, *100*, 127802.
- (10) Garbui, V.; Andreani, C.; Imberti, S.; Pietropaolo, A.; Reiter, G. F.; Senesi, R.; Ricci, M. A. Proton quantum coherence observed in water confined in silica nanopores. *J. Chem. Phys.* **2007**, *127*, 154501.
- (11) Homouz, D.; Reiter, G.; Eckert, J.; Mayers, J.; Blinc, R. Measurement of the 3D Born-Oppenheimer Potential of a Proton in a Hydrogen-Bonded System via Deep Inelastic Neutron Scattering: The Superprotonic Conductor  $\text{Rb}_3\text{H}(\text{SO}_4)_2$ . *Phys. Rev. Lett.* **2007**, *98*, 115502.
- (12) Senesi, R.; Pietropaolo, A.; Bocedi, A.; Pagnotta, S. E.; Bruni, F. Proton Momentum Distribution in a Protein Hydration Shell. *Phys. Rev. Lett.* **2007**, *98*, 138102.
- (13) Morrone, J. A.; Srinivasan, V.; Sebastiani, D.; Car, R. Proton momentum distribution in water: an open path integral molecular dynamics study. *J. Chem. Phys.* **2007**, *126*, 234504.
- (14) Morrone, J. A.; Car, R. Nuclear quantum effects in water. *Phys. Rev. Lett.* **2008**, *101*, 017801.
- (15) Morrone, J. A.; Lin, L.; Car, R. Tunneling and delocalization effects in hydrogen bonded systems: A study in position and momentum space. *J. Chem. Phys.* **2009**, *130*, 204511.
- (16) Ceriotti, M.; Bussi, G.; Parrinello, M. Nuclear Quantum Effects in Solids Using a Colored-Noise Thermostat. *Phys. Rev. Lett.* **2009**, *103*, 030603.
- (17) Ceriotti, M.; Miceli, G.; Pietropaolo, A.; Colognesi, D.; Nale, A.; Catti, M.; Bernasconi, M.; Parrinello, M. Nuclear quantum effects in ab initio dynamics: Theory and experiments for lithium imide. *Phys. Rev. B* **2010**, *82*, 174306.
- (18) Lin, L.; Morrone, J. A.; Car, R.; Parrinello, M. Momentum distribution, vibrational dynamics, and the potential of mean force in ice. *Phys. Rev. B* **2011**, *83*, 220302.

- (19) Perez, A.; Tuckerman, M. E. Improving the convergence of closed and open path integral molecular dynamics via higher order Trotter factorization schemes. *J. Chem. Phys.* **2011**, *135*, 064104.
- (20) Fierke, C. A.; Johnson, K. A.; Benkovic, S. J. Construction and evaluation of the kinetic scheme associated with dihydrofolate reductase from *Escherichia coli*. *Biochemistry* **1987**, *26*, 4085.
- (21) Rajagopalan, P.; Lutz, S.; Benkovic, S. Coupling interactions of distal residues enhance dihydrofolate reductase catalysis: mutational effects on hydride transfer rates. *Biochemistry* **2002**, *41*, 12618.
- (22) Sikorski, R. S.; Wang, L.; Markham, K. A.; Rajagopalan, P. T. R.; Benkovic, S. J.; Kohen, A. Tunneling and coupled motion in the *E. coli* dihydrofolate reductase catalysis. *J. Am. Chem. Soc.* **2004**, *126*, 4778.
- (23) Wang, L.; Tharp, S.; Selzer, T.; Benkovic, S. J.; Kohen, A. Effects of a distal mutation on active site chemistry. *Biochemistry* **2006**, *45*, 1383.
- (24) Wang, L.; Goodey, N. M.; Benkovic, S. J.; Kohen, A. Coordinated Effects of Distal Mutations on Environmentally Coupled Tunneling in Dihydrofolate Reductase. *Proc. Natl. Acad. Sci. U.S.A.* **2006**, *103*, 15753.
- (25) Wang, L.; Goodey, N. M.; Benkovic, S. J.; Kohen, A. The role of enzyme dynamics and tunneling in catalyzing hydride transfer: Studies of distal mutants of dihydrofolate reductase. *Philos. Trans. R. Soc. London, B* **2006**, *361*, 1307.
- (26) Stojković, V.; Perissinotti, L. L.; Lee, J.; Benkovic, S. J.; Kohen, A. The effect of active-site isoleucine to alanine mutation on the DHFR catalyzed hydride-transfer. *Chem. Commun.* **2010**, *46*, 8974.
- (27) Stojković, V.; Perissinotti, L. L.; Lee, J.; Benkovic, S. J.; Kohen, A. *J. Am. Chem. Soc.* **2012**, *134*, 1738.
- (28) Garcia-Viloca, M.; Truhlar, D. G.; Gao, J. Reaction-Path Energetics and Kinetics of the Hydride Transfer Reaction Catalyzed by Dihydrofolate Reductase. *Biochemistry* **2003**, *42*, 13558.
- (29) Pu, J.; Ma, S.; Gao, J.; Truhlar, D. G. Small Temperature Dependence of the Kinetic Isotope Effect for the Hydride Transfer Reaction Catalyzed by *Escherichia coli* Dihydrofolate Reductase. *J. Phys. Chem. B* **2005**, *109*, 8551.
- (30) Pu, J.; Ma, S.; Garcia-Viloca, M.; Gao, J.; Truhlar, D. G.; Kohen, A. Nonperfect Synchronization of Reaction Center Rehybridization in the Transition State of the Hydride Transfer Catalyzed by Dihydrofolate Reductase. *J. Am. Chem. Soc.* **2005**, *127*, 14879.
- (31) Liu, H.; Warshel, A. The Catalytic Effect of Dihydrofolate Reductase and Its Mutants Is Determined by Reorganization Energies. *Biochemistry* **2007**, *46*, 6011.
- (32) Liu, H.; Warshel, A. Origin of the Temperature Dependence of Isotope Effects in Enzymatic Reactions: The Case of Dihydrofolate Reductase. *J. Phys. Chem. B* **2007**, *111*, 7852.
- (33) Agarwal, P. K.; Billeter, S. R.; Hammes-Schiffer, S. Nuclear quantum effects and enzyme dynamics in dihydrofolate reductase catalysis. *J. Phys. Chem. B* **2002**, *106*, 3283.
- (34) Hammes-Schiffer, S. Quantum-classical simulation methods for hydrogen transfer in enzymes: a case study of dihydrofolate reductase. *Curr. Opin. Struct. Biol.* **2004**, *2004*, 192.
- (35) Thorpe, I. F.; Brooks, C. L. Barriers to Hydride Transfer in Wild Type and Mutant Dihydrofolate Reductase from *E. coli*. *J. Phys. Chem. B* **2003**, *107*, 14042.
- (36) Doron, D.; Major, D. T.; Kohen, A.; Thiel, W.; Wu, X. Hybrid Quantum and Classical Simulations of the Dihydrofolate Reductase Catalyzed Hydride Transfer Reaction on an Accurate Semi-Empirical Potential Energy Surface. *J. Chem. Theory Comput.* **2011**, *7*, 3420.
- (37) Boekelheide, N.; Salomón-Ferrer, R.; Miller, T. F. III. Dynamics and dissipation in enzyme catalysis. *Proc. Natl. Acad. Sci. U. S. A.* **2011**, *108*, 16159.
- (38) Major, D. T.; Gao, J. L. Implementation of the bisection sampling method in path integral simulations. *J. Mol. Graphics Modell.* **2005**, *24*, 121.
- (39) Major, D. T.; Garcia-Viloca, M.; Gao, J. Path integral simulations of proton transfer reactions in aqueous solution using combined QM/MM potentials. *J. Chem. Theory Comput.* **2006**, *2*, 236.
- (40) Major, D. T.; Gao, J. A combined quantum mechanical and molecular mechanical study of the reaction mechanism and alpha-amino acidity in alanine racemase. *J. Am. Chem. Soc.* **2006**, *128*, 16345.
- (41) Major, D. T.; Gao, J. An integrated path integral and free-energy perturbation-umbrella sampling method for computing kinetic isotope effects of chemical reactions in solution and in enzymes. *J. Chem. Theory Comput.* **2007**, *3*, 949.
- (42) Rubinstein, A.; Major, D. T. Catalyzing Racemizations in the Absence of a Cofactor: The Reaction Mechanism in Proline Racemase. *J. Am. Chem. Soc.* **2009**, *131*, 8513.
- (43) Major, D. T.; Heroux, A.; Orville, A. M.; Valley, M. P.; Fitzpatrick, P. F.; Gao, J. Differential quantum mechanical tunneling in the uncatalyzed and in the Nitroalkane Oxidase proton abstraction of nitroethane. *Proc. Natl. Acad. Sci. U. S. A.* **2009**, *106*, 20734.
- (44) Azuri, A.; Engel, H.; Doron, D.; Major, D. T. Path-Integral Calculations of Nuclear Quantum Effects in Model Systems, Small Molecules, and Enzymes via Gradient Based Forward Corrector Algorithms. *J. Chem. Theory Comput.* **2011**, *7*, 1273.
- (45) Ceperley, D. M.; Pollock, E. L. The momentum distribution of normal and superfluid liquid  $^4\text{He}$ . *Can. J. Phys.* **1987**, *65*, 1416.
- (46) Ceperley, D. M., The Momentum Distribution of  $^4\text{He}$  at Non-zero Temperature. In *Momentum Distributions*; Silver, R. N., Sokol, P. E., Eds.; Plenum Press: New York, 1989.
- (47) Hwang, J. K.; Chu, Z. T.; Yadav, A.; Warshel, A. Simulations of quantum-mechanical corrections for rate constants of hydride-transfer reactions in enzymes and solutions. *J. Phys. Chem.* **1991**, *95*, 8445.
- (48) Hwang, J. K.; Warshel, A. A quantized classical path approach for calculations of quantum-mechanical rate constants. *J. Phys. Chem.* **1993**, *97*, 10053.
- (49) Warshel, A.; Levitt, M. Theoretical Studies of Enzymatic Reactions - Dielectric, Electrostatic and Steric Stabilization of Carbonium-Ion in Reaction of Lysozyme. *J. Mol. Biol.* **1976**, *103*, 227.
- (50) Sprik, M.; Klein, M. L.; Chandler, D. Staging - a sampling technique for the monte-carlo evaluation of path-integrals. *Phys. Rev. B* **1985**, *31*, 4234.
- (51) Klemm, A. D.; Storer, R. G. Structure of quantum fluids - helium and neon. *Aust. J. Phys.* **1973**, *26*, 43.
- (52) Thirumalai, D.; Berne, B. J. On the calculation of time correlation-functions in quantum-systems - path integral techniques. *J. Chem. Phys.* **1983**, *79*, 5029.
- (53) Thirumalai, D.; Bruskin, E. J.; Berne, B. J. An iterative scheme for the evaluation of discretized path-integrals. *J. Chem. Phys.* **1983**, *79*, 5063.
- (54) Sethia, A.; Sanyal, S.; Singh, Y. Discretized path integral method and properties of a quantum system. *J. Chem. Phys.* **1990**, *93*, 7268.
- (55) Sawaya, M.; Kraut, J. Loop and Subdomain Movements in the Mechanism of *Escherichia coli* Dihydrofolate Reductase: Crystallographic Evidence. *Biochemistry* **1997**, *36*, 586.
- (56) Chen, Y. Q.; Kraut, J.; Blakley, R. L.; Callender, R. Determination by Raman Spectroscopy of the pKa of N5 of Dihydrofolate Bound to Dihydrofolate Reductase: Mechanistic Implications. *Biochemistry* **1994**, *33*, 7021.
- (57) Chen, Y.; Kraut, J.; Callender, R. pH-dependent conformational changes in *Escherichia coli* dihydrofolate reductase revealed by Raman difference spectroscopy. *Biophys. J.* **1997**, *72*, 936.
- (58) Deng, H.; Callender, R. Structure of Dihydrofolate When Bound to Dihydrofolate Reductase. *J. Am. Chem. Soc.* **1998**, *120*, 7730.
- (59) Lipkowitz, K. B.; Boyd, D. B.; Gao, J. In *Methods and Applications of Combined Quantum Mechanical and Molecular Mechanical Potentials*; VCH Publishers: New York, 1995; Vol. 7, pp 119–185.
- (60) Gao, J.; Thompson, M. A. *Combined Quantum Mechanical and Molecular Mechanical Methods*; American Chemical Society: Washington, DC, 1998; Vol. 712.
- (61) Dewar, M. J. S.; Zuebis, E. G.; Healy, E. F.; Stewart, J. J. P. AM1: a new general purpose quantum mechanical molecular model. *J. Am. Chem. Soc.* **1985**, *107*, 3902.
- (62) MacKerell, A. D.; Bashford, D.; Bellott, D.; Dunbrack, R. L.; Evanseck, J. D.; Field, M. J.; Fischer, S.; Gao, J.; Guo, H.; Ha, S.;



Joseph-McCarthy, D.; Kuchnir, L.; Kuczera, K.; Lau, F. T. K.; Mattos, C.; Michnick, S.; Ngo, T.; Nguyen, D. T.; Prodhom, B.; Reiher, W. E.; Roux, B.; Schlenkrich, M.; Smith, J. C.; Stote, R.; Straub, J.; Watanabe, M.; Wiorkiewicz-Kuczera, J.; Yin, D.; Karplus, M. All-Atom Empirical Potential for Molecular Modeling and Dynamics Studies of Proteins. *J. Phys. Chem. B* **1998**, *102*, 3586.

(63) MacKerell, A. D.; Feig, M.; Brooks, C. L. III. Extending the treatment of backbone energetics in protein force fields: Limitations of gas-phase quantum mechanics in reproducing protein conformational distributions in molecular dynamics simulations. *J. Comput. Chem.* **2004**, *25*, 1400.

(64) Jorgensen, W. L.; Chandrasekhar, J.; Madura, J. D.; Impey, R. W.; Klein, M. L. Comparison of simple potential functions for simulating liquid water. *J. Chem. Phys.* **1983**, *79*, 926.

(65) Gao, J. Toward a Molecular Orbital Derived Empirical Potential for Liquid Simulations. *J. Phys. Chem. B* **1997**, *101*, 657.

(66) Nam, K.; Gao, J.; York, D. M. An Efficient Linear-Scaling Ewald Method for Long-Range Electrostatic Interactions in Combined QM/MM Calculations. *J. Chem. Theory Comput.* **2005**, *1*, 2.

(67) Andersen, H. C. Molecular dynamics simulations at constant pressure and/or temperature. *J. Chem. Phys.* **1980**, *72*, 2384.

(68) Hoover, W. G. Canonical dynamics: Equilibrium phase-space distributions. *Phys. Rev. A: At., Mol., Opt. Phys.* **1985**, *31*, 1695.

(69) Hockney, R. The potential calculation and some applications. *Methods Comput. Phys.* **1970**, *9*.

(70) Ryckaert, J.-P.; Ciccotti, G.; Berendsen, H. J. C. Numerical integration of the cartesian equations of motion of a system with constraints: molecular dynamics of n-alkanes. *J. Comput. Phys.* **1977**, *23*, 327.

(71) Pu, J.; Gao, J.; Truhlar, D. G. Multidimensional Tunneling, Recrossing, and the Transmission Coefficient for Enzymatic Reactions. *Chem. Rev.* **2006**, *106*, 3140.

(72) Torrie, G. M.; Valleau, J. P. Nonphysical sampling distributions in Monte Carlo free-energy estimation: Umbrella sampling. *J. Comput. Phys.* **1977**, *23*, 187.

(73) Brooks, B. R.; Bruccoleri, R. E.; Olafson, B. D.; States, D. J.; Swaminathan, S.; Karplus, M. CHARMM: A Program for Macromolecular Energy, Minimization, and Dynamics Calculations. *J. Comput. Chem.* **1983**, *4*, 187.

(74) Brooks, B. R.; Iii, C. L. B.; Mackerell, A. D.; Nilsson, L.; Petrella, R. J.; Roux, B.; Won, Y.; Archontis, G.; Bartels, C.; Boresch, S.; Caflisch, A.; Caves, L.; Cui, Q.; Dinner, A. R.; Feig, M.; Fischer, S.; Gao, J.; Hodoscek, M.; Im, W.; Kuczera, K.; Lazaridis, T.; Ma, J.; Ovchinnikov, V.; Paci, E.; Pastor, R. W.; Post, C. B.; Pu, J. Z.; Schaefer, M.; Tidor, B.; Venable, R. M.; Woodcock, H. L.; Wu, X.; Yang, W.; York, D. M.; Karplus, M. CHARMM: The Biomolecular Simulation Program. *J. Comput. Chem.* **2009**, *30*, 1545.

(75) Kamerlin, S. C. L.; Mavri, J.; Warshel, A. Examining the case for the effect of barrier compression on tunneling, vibrationally enhanced catalysis, catalytic entropy and related issues. *FEBS Lett.* **2010**, *584*, 2759.

(76) Lin, L.; Morrone, J. A.; Car, R. Correlated Tunneling in Hydrogen Bonds. *J. Stat. Phys.* **2011**, *145*, 365.

#### ■ NOTE ADDED AFTER ASAP PUBLICATION

This article was published ASAP on March 14, 2012. In the Theory section, the font of some Greek characters has been changed. The correct version was published on March 20, 2012.